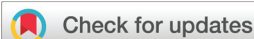


## RESEARCH ARTICLE



Cite this: *Inorg. Chem. Front.*, 2017, **4**, 1337

# Synthesis, crystal structures, and electronic properties of one dimensional $\text{Ba}_9\text{Sn}_3(\text{Te}_{1-x}\text{Se}_x)_{15}$ ( $x = 0-1$ )<sup>†</sup>

Jun Zhang,<sup>a,b</sup> Rui Su,<sup>c</sup> Xiancheng Wang,<sup>\*a,b</sup> Wenmin Li,<sup>a,b</sup> Jianfa Zhao,<sup>a,b</sup> Zheng Deng,<sup>a,b</sup> Sijia Zhang,<sup>a,b</sup> Shaomin Feng,<sup>a,b</sup> Qingqing Liu,<sup>a,b</sup> Huaizhou Zhao,<sup>a,b</sup> Pengfei Guan<sup>\*c</sup> and Changqing Jin<sup>\*a,b,d,e</sup>

In this work, the  $\text{Ba}_9\text{Sn}_3\text{Te}_{15}$  compound has been synthesized for the first time under high pressure and high temperature conditions. Single-crystal X-ray diffraction analysis shows that  $\text{Ba}_9\text{Sn}_3\text{Te}_{15}$  crystallizes into a hexagonal structure with a space group of  $P6c2$  (188) and lattice parameters of  $a = b = 10.2403(1)$  Å, and  $c = 20.7720(2)$  Å. The crystal structure contains trimeric one-dimensional chains with face-sharing  $\text{SnTe}_6$  octahedrons stacked along the  $c$ -axis. These chains are arranged in a triangular lattice in the  $ab$  plane. The energy dispersive X-ray spectroscopy measurement for a single crystal of  $\text{Ba}_9\text{Sn}_3\text{Te}_{15}$  shows approximately 6% vacancies on the Sn sites. The anion Te can be substituted by Se to form  $\text{Ba}_9\text{Sn}_3(\text{Te}_{1-x}\text{Se}_x)_{15}$  with  $x = 0-1$ . The resistivity and Seebeck coefficient measurements were performed.  $\text{Ba}_9\text{Sn}_3\text{Te}_{15}$  behaves similar to a semiconductor with a band gap of approximately 24 meV. When Se is doped, the resistivity increases and the band gap is enhanced to 508 meV for  $x = 1$ . The Seebeck coefficient ranges from  $31 \mu\text{V K}^{-1}$  to  $90.7 \mu\text{V K}^{-1}$ . *Ab initio* calculations were also performed to study the density of states and band structures for  $\text{Ba}_9\text{Sn}_3\text{Te}_{15}$  and  $\text{Ba}_9\text{Sn}_3\text{Se}_{15}$ .

Received 23rd April 2017,  
Accepted 18th June 2017

DOI: 10.1039/c7qi00219j

rsc.li/frontiers-inorganic

## Introduction

Research on thermoelectric materials has received considerable attention because of their potential applications in the field of energy conversion.<sup>1</sup> To improve the efficiency of thermoelectric materials (as determined by  $ZT = (S^2\sigma/\kappa)T$ ), numerous strategies have been developed to increase the Seebeck coefficient  $S$  and electrical conductivity  $\sigma$ , as well as decrease the thermal conductivity  $\kappa$ .<sup>2</sup> Extensive efforts have been focused recently on the “old material” called tin chalcogenides due to their ultralow thermal conductivity and extremely high thermoelectric figure of merit reported in SnSe single crystals.<sup>3</sup> p-Type SnSe was synthesized by introducing different hole

dopants to study the effect of doping on the thermoelectric performance. The record high  $ZT_{\text{dev}}$  (device dimensionless figure of merit) of approximately 1.34 has been realized in Na-doped SnSe.<sup>4</sup> Before SnSe was extensively studied, Assoud *et al.* reported the synthesis of  $\text{Ba}_2\text{SnTe}_5$ ,  $\text{Ba}_2\text{SnSe}_5$ , and  $\text{Ba}_7\text{Sn}_3\text{Se}_{13}$ , as well as studied their performance to search for new thermoelectric materials in the tin chalcogenide family.<sup>5</sup> Undoped  $\text{Ba}_2\text{SnTe}_5$  was reported to be a p-type semiconductor with a band gap of approximately 0.18 eV and a Seebeck coefficient of approximately  $560 \mu\text{V K}^{-1}$  at room temperature. Accordingly, undoped  $\text{Ba}_2\text{SnTe}_5$  was suggested to be a good candidate as a thermoelectric material. However, the band gaps of the other two tin chalcogenides exceeded 1 eV and were excessively high for a thermoelectric material.

This study reports a new member of the alkaline earth tin chalcogenides  $\text{Ba}_9\text{Sn}_3\text{Te}_{15}$ , which was synthesized under high pressure conditions. The distinctive feature of the crystal structure is the presence of trimeric face-sharing  $\text{SnTe}_6$  octahedral chains along the  $c$  direction, thereby leading to a one-dimensional electronic structure for this compound. Te atoms in  $\text{Ba}_9\text{Sn}_3(\text{Te}_{1-x}\text{Se}_x)_{15}$  can be completely substituted with Se to form the end-point compound  $\text{Ba}_9\text{Sn}_3\text{Se}_{15}$ . All  $\text{Ba}_9\text{Sn}_3(\text{Te}_{1-x}\text{Se}_x)_{15}$  compounds with  $x = 0-1$  are semiconductors with a band gap and Seebeck coefficient that range from 24 meV to 508 meV and  $31 \mu\text{V K}^{-1}$  to  $90.7 \mu\text{V K}^{-1}$ , respectively.

<sup>a</sup>Beijing National Laboratory for Condensed Matter Physics, Institute of Physics, Chinese Academy of Sciences, Beijing 100190, China

<sup>b</sup>University of Chinese Academy of Sciences, Beijing 100049, China.

E-mail: wangxiancheng@iphy.ac.cn

<sup>c</sup>Beijing Computational Science Research Center, Beijing 100193, China.

E-mail: pguan@csrc.ac.cn

<sup>d</sup>Collaborative Innovation Center of Quantum Matter, Beijing 100190, China

<sup>e</sup>School of Physical Sciences, University of Chinese Academy of Sciences,

Beijing 100190, China. E-mail: jin@iphy.ac.cn

<sup>†</sup>Electronic supplementary information (ESI) available. CCDC 1557111. For ESI and crystallographic data in CIF or other electronic format see DOI: 10.1039/c7qi00219j

## Experiments and calculations

### Sample synthesis

Commercially available crystalline powders of Sn (Alfa, 99.995% pure) and Se (Alfa, 99.999% pure), and lumps of Ba (Alfa, immersed in oil, >99.2% pure) and Te (Alfa, 99.999% pure) were used as starting materials.  $\text{Ba}_9\text{Sn}_3\text{Te}_{15}$  single crystal was prepared under high pressure and temperature conditions. The precursor BaTe was prepared through the reaction of the Ba blocks and Te powder in an alumina crucible sealed in an evacuated quartz tube at 700 °C for 20 h. The mixture of BaTe, Sn, and Te was homogeneously mixed based on a molar ratio 3:1:2 and pressed into a pellet with a diameter of 6 mm. The pre-pressed pellet was placed in an h-BN capsule and into a graphite tube furnace thereafter. High pressure experiments were performed in a DS6 × 600 T cubic anvil high-pressure apparatus. After the pressure was gradually increased to 5.5 GPa, the system was heated to 1500 °C within 4 min and maintained for 40 min. Moreover, the temperature was controlled to decrease to 1000 °C in 3 h and quenched to room temperature thereafter. After the high pressure and high temperature process, the bright single crystalline sample of  $\text{Ba}_9\text{Sn}_3\text{Te}_{15}$  was obtained. Polycrystalline samples of  $\text{Ba}_9\text{Sn}_3(\text{Te}_{1-x}\text{Se}_x)_{15}$  ( $x = 0-1$ ) were synthesized by a similar process without the slow cooling process.

### Characterization

Single crystal X-ray diffraction measurement was performed at 299.6(5) K on an APEX III CCD diffractometer using monochromatic Mo K $\alpha$  radiation ( $\lambda = 0.71073$  Å). The structure was resolved through the Patterson methods and refined by full-matrix least-squares fitting on  $F^2$ . All calculations were performed using programs from the Olex2 crystallographic software package.<sup>6</sup> The structure was verified using PLATON for the missing symmetry elements.<sup>7</sup> Powder X-ray diffraction was performed on a Rigaku Ultima VI (3KW) diffractometer using Cu K $\alpha$  radiation generated at 40 kV and 40 mA. The X-ray data were collected at a scanning rate of 1° per min and a scanning step length of 0.02 degrees. Rietveld refinement on the diffraction spectra was performed using Gsas software packages. Resistivity was measured using a physical property measuring system (PPMS). The Seebeck coefficient was measured at room temperature using a commercial thermopower measurement apparatus. The chemical compositions of the  $\text{Ba}_9\text{Sn}_3\text{Te}_{15}$  single crystal were determined through energy dispersive X-ray spectroscopy (EDX).

### Theoretical calculations

*Ab initio* calculations were performed using the Vienna *ab initio* simulation package (VASP).<sup>8</sup> The valence ion interactions were described through projector augmented wave (PAW) potentials.<sup>8,9</sup> The valence wave functions were expanded using a plane-wave basis up to a kinetic energy cutoff of 350 eV for all calculations. A primitive cell of  $\text{Ba}_9\text{Sn}_3\text{Te}/\text{Se}_{15}$  that comprises 54 atoms was constructed from the Rietveld analysis results. A complete optimization of the lattice cell and atom

positions was performed with a force tolerance of 0.02 eV Å<sup>-1</sup>. The Perdew, Burke, Ernzerhof (PBE) functional<sup>10</sup> and a Monkhorst–Pack  $K$ -points mesh of  $5 \times 5 \times 3$  were used for the structural optimization. The optimization yields the lattice parameters changed to  $a = 10.4200(0)$  Å,  $c = 21.0600(0)$  Å for  $\text{Ba}_9\text{Sn}_3\text{Te}_{15}$  and  $a = 9.7900(0)$  Å,  $c = 19.9700(0)$  Å for  $\text{Ba}_9\text{Sn}_3\text{Se}_{15}$ , respectively. Thereafter, electronic structure calculation was performed based on the PBE optimized structure. Given the well-known inaccuracy of the PBE functional for semiconductors, the hybrid Heyd–Scuseria–Ernzerhof (HSE06) functional<sup>11</sup> was employed for the electron structure calculation. For the HSE calculation, a  $K$ -point mesh of  $5 \times 5 \times 5$  and additional 64 empty bands were used. A Gaussian smearing of 0.1 eV was used for the Brillouin integration. Wannier interpolation<sup>12</sup> was employed to obtain the band structure.

## Results and discussion

The single crystal  $\text{Ba}_9\text{Sn}_3\text{Te}_{15}$  was grown under high-pressure conditions. These crystals present a needle shape with a typical length of approximately 400  $\mu\text{m}$  (see the inset of Fig. 1). The chemical compositions of  $\text{Ba}_9\text{Sn}_3\text{Te}_{15}$  as measured by EDX on single crystals are shown in Fig. 1. In order to ensure more accuracy, several crystals were used and EDX measurement was carried out on the crystal surfaces, more than twenty different areas and took the average. The average atomic ratio of Ba : Sn : Te is approximately 3.00(0) : 0.94(3) : 5.10(4), which is nearly 3 : 1 : 5, thereby suggesting approximately 6% vacancy on the Sn sites. Excessive Te atoms may be derived from the small impurities on the surface of the single crystal.

Single crystal XRD data of  $\text{Ba}_9\text{Sn}_3\text{Te}_{15}$  were collected, and the crystal structure of the new material was resolved. The refinement smoothly converged to  $F^2 = 1.188$ ,  $R_1 = 0.028$ , and  $wR_2 = 0.056$ . Table 1 summarizes parts of the refinement results.  $\text{Ba}_9\text{Sn}_3\text{Te}_{15}$  crystallizes into a hexagonal structure with the space group of  $P\bar{6}c2$  (188), and  $\text{Ba}_9\text{Fe}_3\text{S}_{15}$  is the prototype structure.<sup>13</sup> The lattice constants are  $a = b = 10.2403(1)$  Å and  $c = 20.7720(2)$  Å. The sketch of the crystal structure is plotted, and Fig. 2(a) and (b) show the top view with the projection along the  $c$  axis and the perspective view with the projection along the [110] direction, respectively. Evidently,  $\text{Ba}_9\text{Sn}_3\text{Te}_{15}$  is constructed with face-sharing octahedral  $\text{SnTe}_6$  chains that are

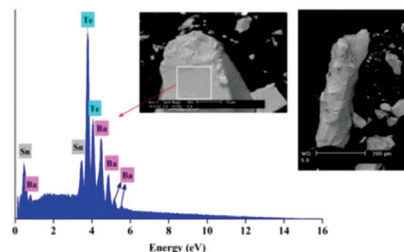


**Fig. 1** Energy dispersive X-ray spectrum collected on typical  $\text{Ba}_9\text{Sn}_3\text{Te}_{15}$  single crystals.

**Table 1** Crystallographic data for Ba<sub>9</sub>Sn<sub>3</sub>Te<sub>15</sub>

Formula: Ba<sub>9</sub>Sn<sub>3</sub>Te<sub>15</sub>  
 Space group:  $P\bar{6}c2$ ; temperature/K: 299.6(5);  
 $a = b = 10.2403(1)$  Å,  $c = 20.7720(2)$  Å;  $\alpha = \beta = 90^\circ$ ,  $\gamma = 120^\circ$ ;  
 $V = 1886.4(4)$  Å<sup>3</sup>;  $Z = 2$ ;  
 Goodness-of-fit on  $F^2$ : 1.18(8);  
 Final  $R$  indexes [all data]:  $R_1 = 0.028(4)$ ,  $wR_2 = 0.056(6)$

## Atomic parameters

Atom	Wyck.	$x$	$y$	$z$	Occ.
Ba1	12l	0.3774(1)	0.3876(2)	0.0833(2)	1
Ba2	6k	-0.0222(9)	0.3690(9)	0.2500(0)	1
Sn1	2a	0.0000(0)	0.0000(0)	0.0000(0)	1
Sn2	4g	0.0000(0)	0.0000(0)	0.1661(6)	0.96(4)
Te1	12l	-0.0027(4)	0.2497(2)	0.0837(5)	1
Te2	6k	0.2447(0)	0.2574(4)	0.2500(0)	1
Te3	2c	0.3333(3)	0.6666(7)	0.0000(0)	1
Te4	4h	0.3333(3)	0.6666(7)	0.1830(3)	1
Te5	4i	0.6666(7)	0.3333(3)	0.1559(9)	1
Te6	4i	0.6666(7)	0.3333(3)	0.0081(0)	0.5

## Bond length

Sn(1)–Te(1)	3.10(4) Å	Sn(2)–Te(2)	3.10(7) Å
Sn(2)–Te(1)	3.08(9) Å		
Te(4)–Te(4)	2.78(2) Å	Te(5)–Te(6)	3.07(1) Å

## The distance of adjacent atoms

Sn(1)–Sn(2)	3.45(3) Å	Sn(2)–Sn(2)	3.48(4) Å
Te(3)–Te(4)	3.80(3) Å	Te(5)–Te(5)	3.91(5) Å

## Bond angle

Te(1)–Sn(1)–Te(1)	179(1)°	Te(1)–Sn(2)–Te(2)	178(3)°
-------------------	---------	-------------------	---------

arranged in a triangular lattice in the  $ab$  plane. The SnTe<sub>6</sub> chains are trimeric along the  $c$ -axis, thereby resulting in two sites of Sn(1) at (0, 0, 0) and Sn(2) at (0, 0,  $z$ ). The refinements yield an occupation rate of approximately 96% on the Sn(2) site. Given the atomic ratio of Sn(1) to Sn(2) of 1 : 2, the total occupation rate of Sn should be approximately 97%, which is near the EDX measurement result of 94%. Apart from the SnTe<sub>6</sub> chains, two Te chains are located in the centers of the triangular lattices, that is the (1/3, 2/3,  $x$ ) and (2/3, 1/3,  $y$ ) sites. For the sites occupied by the Te(6) atoms, the occupation ratio is 0.5.

In a trimer unit, two Sn atoms are on the Sn(2) site and one is on the Sn(1) site (see Fig. 3). This study attempts to define the degree of trimerization using the ratio of ( $|d_{\text{inter}} - d_{\text{intra}}| : |d_{\text{inter}} + d_{\text{intra}}|$ ), where  $d_{\text{inter}}$  is the distance of the adjacent Sn(2) atoms and  $d_{\text{intra}}$  is that of the adjacent Sn(1) and Sn(2) atoms. The crystallographic parameters presented in Table 1 enable us to calculate the trimerization degree as approximately 0.4%, which is less than that of Ba<sub>9</sub>Fe<sub>3</sub>S<sub>15</sub> (*i.e.*, 3.3%) as evaluated from ref. 13. In the SnTe<sub>6</sub> octahedron, the bond angles Te(1)–Sn(1)–Te(1) and Te(1)–Sn(2)–Te(2) are 179° and 178°, respectively, which deviated from the value of 180° in a regular octahedron. This result indicates that the SnTe<sub>6</sub> octahedron was slightly distorted. The Sn–Te bond lengths were between 3.08 and 3.10 Å, which are relatively less than the Sn–Te distances of 3.16 Å in the SnTe compound.<sup>14</sup>

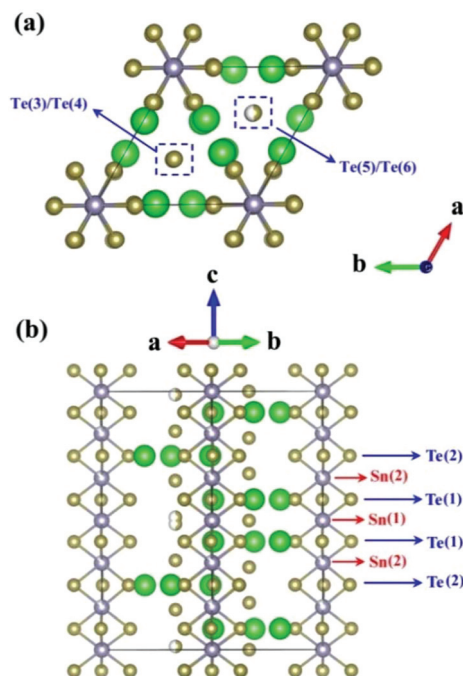


**Fig. 2** The sketch of the crystal structure of Ba<sub>9</sub>Sn<sub>3</sub>Te<sub>15</sub>, showing the face-sharing octahedral SnTe<sub>6</sub> chains arranged in a triangular lattice in the  $ab$ -plane. (a) is the top view with the projection along the  $c$  axis; (b) is the perspective view with the projection along the [110] direction.

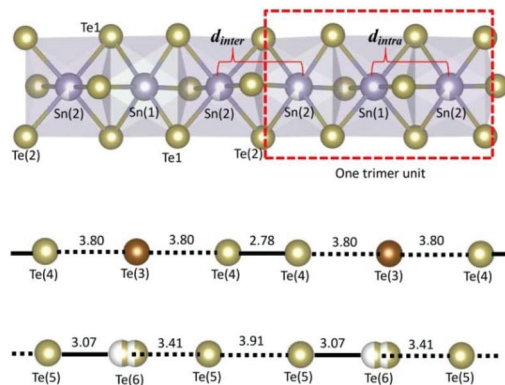


**Fig. 3** The sketch of SnTe<sub>6</sub> octahedral chains and Te chains in the compound of Ba<sub>9</sub>Sn<sub>3</sub>Te<sub>15</sub>.

The sketch of the Te chains composed of the Te(3)–Te(4) and Te(5)–Te(6) atoms is presented in Fig. 3. The distance of the adjacent Te atoms in the Te chains ranges from 2.78 Å to 3.91 Å. In polytellurides, the Te atoms can form bonds with each other, with the bond length ranging from 2.70 Å to 3.10 Å. The case of Rb<sub>2</sub>Te<sub>5</sub> and Cs<sub>2</sub>Te<sub>5</sub> presented the square-planar Te<sub>5</sub> unit chains. In these chains, the charge of the Te<sub>5</sub> unit is –2, and the Te atoms are bonded with the bond lengths approximately 2.76 Å and 3.05 Å.<sup>15</sup> For the bent Te<sub>5</sub><sup>4–</sup> unit in Ba<sub>2</sub>SnTe<sub>5</sub>, the Te–Te bond lengths range from 2.81 Å to

3.10 Å.<sup>5a</sup> In the Te chains of Ba<sub>9</sub>Sn<sub>3</sub>Te<sub>15</sub>, the small distances of Te(5)–Te(6) (3.07 Å) and Te(4)–Te(4) (2.78 Å) suggest that dimeric Te<sub>2</sub><sup>2-</sup> units are formed. Evidently, 2/3 of the Te atoms in the Te chains are dimerized (see Fig. 3). Thus, based on the site symmetry and charge balance, when the small vacancies on the Sn(2) sites are disregarded, we can reasonably speculate that the molecular formula can be rewritten as Ba<sup>2+</sup><sub>9</sub>Sn<sup>4+</sup><sub>3</sub>Sn<sup>2+</sup><sub>2</sub>Te<sup>2-</sup><sub>9</sub>(Te<sup>1-</sup><sub>4</sub>Te<sup>2-</sup><sub>2</sub>), where the Sn<sup>4+</sup> atoms are located on the Sn(1) site, Sn<sup>2+</sup> atoms on the Sn(2) site, and the Te<sup>2-</sup><sub>9</sub> atoms are derived from the SnTe<sub>6</sub> octahedra and the (Te<sup>1-</sup><sub>4</sub>Te<sup>2-</sup><sub>2</sub>) atoms from the Te chains. Thus, the oxidation state of Sn should be +4 and +2 for the Sn(1) and Sn(2) sites, respectively.

The Te atoms in Ba<sub>9</sub>Sn<sub>3</sub>Te<sub>15</sub> can be substituted gradually by Se to form Ba<sub>9</sub>Sn<sub>3</sub>(Te<sub>1-x</sub>Se<sub>x</sub>)<sub>15</sub> with  $x = 0-1$ . The X-ray powder diffraction patterns of Ba<sub>9</sub>Sn<sub>3</sub>(Te<sub>1-x</sub>Se<sub>x</sub>)<sub>15</sub> ( $x = 0-1$ ) obtained at room temperature are shown in Fig. 4a, while the enlarged views are shown in Fig. 4b and c. Apart from several small unknown peaks marked by the arrow, most of the peaks can be indexed with the hexagonal structure. The peaks shift toward a high-angle direction monotonously with the increase of content in the Se dopants. This result demonstrates that the Se atoms are successfully doped into Ba<sub>9</sub>Sn<sub>3</sub>Te<sub>15</sub> and implies that the lattice shrinks with Se doping. The lattice constants  $a$  and  $c$  can be obtained from the XRD refinement data; the Se

doping dependence of  $a$  and  $c$  is shown in Fig. 4d and Table 2. The lattice parameters  $a$  and  $c$  decrease with the Se dopants' increase. For the end-point compound Ba<sub>9</sub>Sn<sub>3</sub>Se<sub>15</sub>, the lattice constants are  $a = 9.7209(3)$  (Å) and  $c = 19.5817(1)$  (Å), thereby resulting in a 15.1% smaller cell volume compared with Ba<sub>9</sub>Sn<sub>3</sub>Te<sub>15</sub>. We also refined the X-ray diffraction data of Ba<sub>9</sub>Sn<sub>3</sub>(Te<sub>1-x</sub>Se<sub>x</sub>)<sub>15</sub> (see Fig. S1–S5 and Tables SV–SIX<sup>†</sup>). It is evident that the total occupation of Sn decreases with the increase of Se dopants. For Ba<sub>9</sub>Sn<sub>3</sub>Se<sub>15</sub>, the total occupation ratio on Sn sites is approximately 0.679(2). Therefore, the molecular formula should be changed to Ba<sub>9</sub>Sn<sub>2+ $\delta$</sub> Se<sub>15</sub>. The trimerization degree for Ba<sub>9</sub>Sn<sub>2+ $\delta$</sub> Se<sub>15</sub> is calculated to be approximately 15.1%, which is larger than that for Ba<sub>9</sub>Sn<sub>3</sub>Te<sub>15</sub>. This result suggests substantial distortion of the SnSe<sub>6</sub> octahedron in Ba<sub>9</sub>Sn<sub>2+ $\delta$</sub> Se<sub>15</sub>.

Resistivity measurements were performed on the polycrystalline Ba<sub>9</sub>Sn<sub>3</sub>(Te<sub>1-x</sub>Se<sub>x</sub>)<sub>15</sub> samples. The temperature dependence of the resistivity is presented in Fig. 5a. For all samples, the resistivity increases with decreasing temperature, thereby demonstrating a behavior similar to semiconductors. Moreover, the resistivity increases rapidly when the Te atoms are substituted by Se. The resistivity for Ba<sub>9</sub>Sn<sub>3</sub>Te<sub>15</sub> in the entire temperature range from 2 K to 350 K and the plot of  $\ln \rho$  versus  $1/T$  are shown in Fig. 5b. The resistivity value is extremely small at 350 K, that is a mere 0.19(6) Ω cm. The

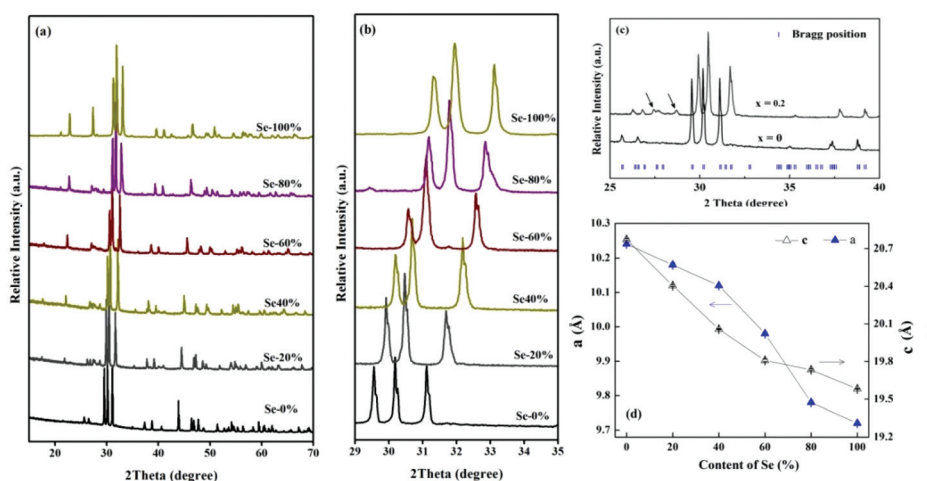


**Fig. 4** (a) X-ray powder diffraction patterns of Ba<sub>9</sub>Sn<sub>3</sub>(Te<sub>1-x</sub>Se<sub>x</sub>)<sub>15</sub> ( $x = 0-1$ ) measured at room temperature; (b) the enlarged view between 29–35 degrees; (c) the enlarged view of XRD patterns for the samples of Ba<sub>9</sub>Sn<sub>3</sub>(Te<sub>1-x</sub>Se<sub>x</sub>)<sub>15</sub>  $x = 0$  and 0.2, the small peaks marked by arrows is from unknown impurities; (d) the lattice constants  $a$  and  $c$  dependent on the Se doping level in Ba<sub>9</sub>Sn<sub>3</sub>(Te<sub>1-x</sub>Se<sub>x</sub>)<sub>15</sub> ( $x = 0-1$ ).

**Table 2** The lattice parameters and total occupation on sn sites for Ba<sub>9</sub>Sn<sub>3</sub>(Te<sub>1-x</sub>Se<sub>x</sub>)<sub>15</sub>

Ba <sub>9</sub> Sn <sub>3</sub> (Te <sub>1-x</sub> Se <sub>x</sub> ) <sub>15</sub>						
Composition ( $x$ )	0	0.2	0.4	0.6	0.8	1
$a$ (Å)	10.2403(1)	10.1850(2)	10.1209(0)	9.9849(7)	9.7846(5)	9.7209(3)
$c$ (Å)	20.7720(2)	20.4055(7)	20.0549(3)	19.8109(0)	19.7325(7)	19.5817(1)
$V$ (Å <sup>3</sup> )	1886.44(0)	1833.17(0)	1779.05(7)	1710.52(1)	1636.08(0)	1602.48(9)
Total occupation on Sn sites	0.973(3)	0.972(8)	0.841(7)	0.820(0)	0.720(2)	0.679(2)

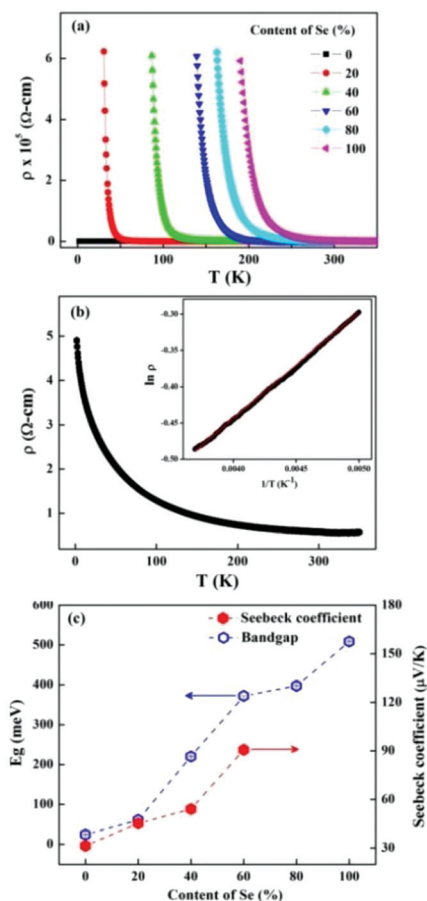


**Fig. 5** (a) The electronic transport properties of  $\text{Ba}_9\text{Sn}_3(\text{Te}_{1-x}\text{Se}_x)_{15}$  ( $x = 0-1$ ) as a function of the content of se; (b) the resistivity as a function of temperature for  $\text{Ba}_9\text{Sn}_3\text{Te}_{15}$ . The inset shows the  $\ln(\rho)$  versus inversed temperature. (c) The Se doping dependence of the band gap and Seebeck coefficient. The resistivity of the samples of  $x = 0.8$  and  $0.1$  is too large for the measurement of the Seebeck coefficient.

$\ln \rho$  versus  $1/T$  curve presents a straight line, thereby suggesting a semiconducting behavior that can be described based on the Arrhenius law for thermally activated conduction. By using the formula,  $R \propto \exp(\Delta_g/2k_B T)$ , where  $\Delta_g$  is the semiconducting band gap and  $k_B$  is the Boltzmann's constant, the resistivity curve is well fitted and  $\Delta_g$  is given to be  $24.4(0)$  meV. By using the same method, band gaps for other doped samples were obtained (see Fig. 5c). The band gap was gradually enhanced by the Se substitution and reached the maximum 508 meV for the end point sample  $\text{Ba}_9\text{Sn}_{2+\delta}\text{Se}_{15}$ . The Seebeck coefficient was measured at room temperature, and the Se doping dependence of the Seebeck coefficient is shown in Fig. 5c. In this study, no Seebeck coefficient data were obtained for the samples with  $x = 0.8$  and  $1.0$  because of the extremely large resistivity for the measurement of the Seebeck coefficient. Similar to the band gap evolution, the Seebeck coefficient increased with increasing Se doping and ranged from  $31 \mu\text{V K}^{-1}$  to  $90.7 \mu\text{V K}^{-1}$ . Compared with those of the most often used thermoelectric  $\text{Bi}_2\text{Te}_3$  ( $>170 \mu\text{V K}^{-1}$ )<sup>16</sup> and extensively studied  $\text{SnSe}$

( $>500 \mu\text{V K}^{-1}$ )<sup>3</sup>, the Seebeck coefficient of  $\text{Ba}_9\text{Sn}_3(\text{Te}_{1-x}\text{Se}_x)_{15}$  is relatively lower for a thermoelectric material.

To obtain in-depth insight into the relationship between the structure and properties, we performed theoretical calculations for the  $\text{Ba}_9\text{Sn}_3\text{Te}_{15}$  and  $\text{Ba}_9\text{Sn}_3\text{Se}_{15}$  compounds. The calculated density of states (DOS) and band structure for  $\text{Ba}_9\text{Sn}_3\text{Te}_{15}$  and  $\text{Ba}_9\text{Sn}_3\text{Se}_{15}$  are shown in Fig. 6. In Fig. 6a, PBE and HSE06 XC functional predict an unoccupied peak at approximately 0.2 eV and a flat region that continually crosses the Fermi level. Thus, the ideal  $\text{Ba}_9\text{Sn}_3\text{Te}_{15}$  would be a poor conductor. The valence band position is overestimated by 0.5 eV by PBE due to the lack of non-local exchange. By contrast, the conduction band is underestimated by approximately the same magnitude. The projected DOS (see Fig. 6a) demonstrates that the unoccupied peak and the flat region are solely contributed by the 5s and 5p orbitals of the Sn-Te chains. To

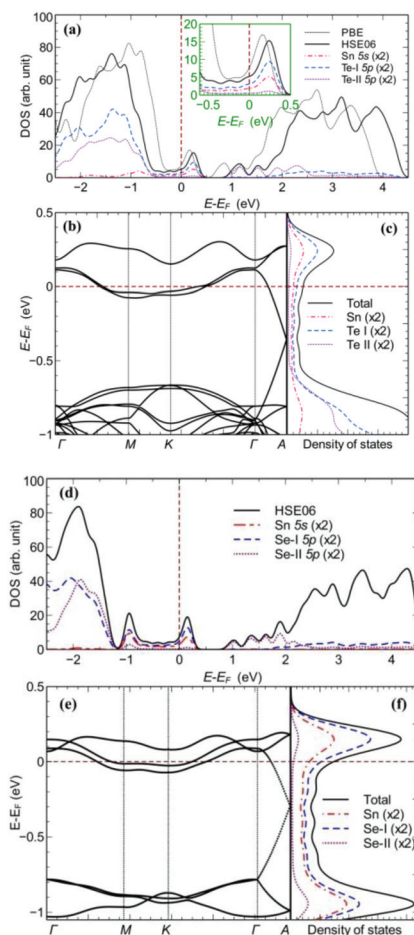


**Fig. 6** The calculated density of states (DOS) and band structure for  $\text{Ba}_9\text{Sn}_3\text{Te}_{15}$  (a-c) and  $\text{Ba}_9\text{Sn}_3\text{Se}_{15}$  (d-f). (a, d) Total and projected density of states. Both PBE (black dashed) and HSE06 (thick black) results are presented for the total DOS. The p and s orbital projected DOS for Te-I or Se-I (blue dashed), Te-II or Se-II (purple dashed) and Sn (pink dotted) are also presented. An enlarged view for the energy close to the Fermi level is shown in (a) in the intersected plot. The projected DOS plots are multiplied by a factor of 20 for comparison purpose. (b, e) The band structure combined with (c, f) DOS.

clarify the origin of the DOS structure, we calculated the HSE band structure using the Wannier interpolation technique (see Fig. 6b). The high-symmetry path can be divided into two parts:  $\Gamma$ - $M$ - $K$ - $\Gamma$ , which is parallel to the  $ab$  plane, and  $\Gamma$ - $A$ , which is perpendicular to the  $ab$  plane. For the in-plane part, the band structure shows a flat valence band (VB) and conduction band (CB) between the M and K points. VB and CB were separated by an indirect gap of 0.6 eV. For the out-plane part, two linear bands crossed at  $-0.4$  eV. The atom-resolved DOS indicates that the two linear bands are produced by the Sn and Te atoms in the chains, thereby exhibiting the quasi one-dimension-like linear bands. To further investigate the real space distribution of the partial occupied bands, we plotted the partial charge density for the energy interval between  $-0.4$  and 0 eV (see Fig. 7). Evidently, the charge is well localized at the Sn-Te chain, thereby presenting clear s and p orbital characters for the Sn and Te atoms, respectively.

The calculated DOS and band structure for  $\text{Ba}_9\text{Sn}_3\text{Se}_{15}$  are shown in Fig. 6(d-f). In general, the band structure remains considerably similar to  $\text{Ba}_9\text{Sn}_3\text{Te}_{15}$  near the Fermi level. Moreover, both compounds show an evident linear band near the A point, which is contributed by the Se-Sn chains. One major difference from the Te situation is the localized band at  $-1$  eV that is induced by the Se-Sn bonding. Compared with the Te situation, where the Te-Sn bonding does not substantially change the VB top of the Te atoms, the formation of the Se-Sn bonding requires substantially high energy to shift the  $p$  electrons of Se out of its valence band. This finding may explain the considerably high Sn holes in the  $\text{Ba}_9\text{Sn}_3\text{Se}_{15}$ .

This section discusses the difference between the experimental and calculated results. The resistivity measurements provide the semiconducting behavior for  $\text{Ba}_9\text{Sn}_3(\text{Te}_{1-x}\text{Se}_x)_{15}$ , which was inconsistent with the poor conducting state predicted by the calculation. However, the Sn sites are not completely occupied for the experimental compound  $\text{Ba}_9\text{Sn}_3\text{X}_{15}$  ( $\text{X} = \text{Se}$  and  $\text{Te}$ ). Given the positively charged Sn, the vacancy of

Sn should induce other Sn ions to lose numerous electrons to balance the charges and act as a hole donor. This scenario could shift the Fermi level downward to below the CB and induce a semiconductor behavior in the  $ab$  plane. Although the linear band (for the out-plane band) crosses the Fermi surface regardless of the Fermi level shift, thereby suggesting the conductivity in the direction of the  $c$ -axis, the one-dimensional conducting behavior can be easily damaged by deficiency because of electron backscattering. Therefore, the  $\text{Ba}_9\text{Sn}_3(\text{Te}_{1-x}\text{Se}_x)_{15}$  compounds would demonstrate semiconductor behavior due to the Sn vacancy.

## Conclusion

The new  $\text{Ba}_9\text{Sn}_3\text{Te}_{15}$  compound with one-dimensional  $\text{SnTe}_6$  octahedral chains was synthesized under high pressure and high temperature conditions. The compound crystallizes into a hexagonal structure with a space group of  $P\bar{6}c2$  (188). The Te atoms can be substituted gradually by Se to form  $\text{Ba}_9\text{Sn}_3(\text{Te}_{1-x}\text{Se}_x)_{15}$ , with  $x = 0-1$ . These compounds are semiconducting, and the band gap increases with the Se doping, which ranges from 24 meV for  $\text{Ba}_9\text{Sn}_3\text{Te}_{15}$  to 508 meV for the end-point compound  $\text{Ba}_9\text{Sn}_3\text{Se}_{15}$ . The Seebeck coefficient for the  $\text{Ba}_9\text{Sn}_3(\text{Te}_{1-x}\text{Se}_x)_{15}$  samples ranges from  $31 \mu\text{V K}^{-1}$  to  $90.7 \mu\text{V K}^{-1}$ . The calculated band structures for  $\text{Ba}_9\text{Sn}_3\text{Te}_{15}$  and  $\text{Ba}_9\text{Sn}_3\text{Se}_{15}$  exhibit quasi one-dimension-like linear bands that correspond to their crystal structure.

## Acknowledgements

This work was financially supported by NSFC and the National Basic Research Program of China.

## References

- (a) M. S. Dresselhaus, G. Chen, M. Y. Tang, R. G. Yang, H. Lee, D. Z. Wang, Z. F. Ren, J. P. Fleurial and P. Gogna, *Adv. Mater.*, 2007, **19**, 1043; (b) G. J. Snyder and E. S. Toberer, *Nat. Mater.*, 2008, **7**, 105.
- (a) J. P. Heremans, V. Jovic, E. S. Toberer, A. Saramat, K. Kurosaki, A. Charoenphakdee, S. Yamanaka and G. J. Snyder, *Science*, 2008, **321**, 554; (b) W. Liu, X. J. Tan, K. Yin, H. J. Liu, X. F. Tang, J. Shi, Q. J. Zhang and C. Uher, *Phys. Rev. Lett.*, 2012, **108**, 166601; (c) J. P. Heremans, C. M. Thrush and D. T. Morelli, *Phys. Rev. B: Condens. Matter*, 2004, **70**, 115334; (d) K. F. Hsu, S. Loo, F. Guo, W. Chen, J. S. Dyck, C. Uher, T. Hogan, E. K. Polychroniadis and M. G. Kanatzidis, *Science*, 2004, **303**, 818.
- L. D. Zhao, S. H. Lo, Y. S. Zhang, H. Sun, G. J. Tan, C. Uher, C. Wolverton, V. P. Dravid and M. G. Kanatzidis, *Nature*, 2014, **508**, 373.
- L. D. Zhao, G. J. Tan, S. Q. Hao, J. Q. He, Y. L. Pei, H. Chi, H. Wang, S. K. Gong, H. B. Xu, V. P. Dravid, C. Uher,

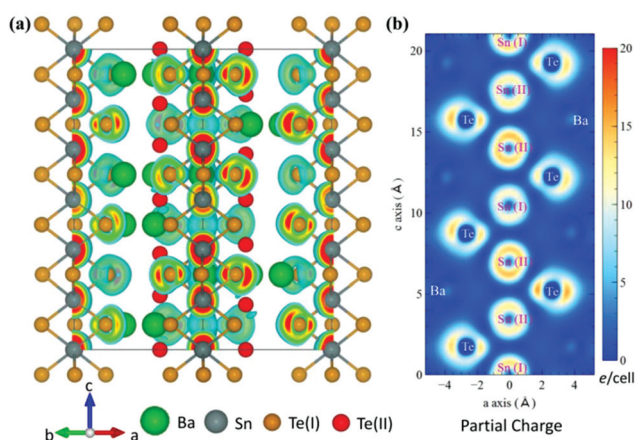


**Fig. 7** Partial charge for the energy range of  $-0.4$  eV to zero. (a)  $\text{Ba}_9\text{Sn}_3\text{Te}_{15}$  structure and iso-surface plot of the partial charge. (b) 2D image of the partial charge distribution on the  $\langle 101 \rangle$  surface. The Sn atom chain is centred at zero.

- G. J. Snyder, C. Wolverton and M. G. Kanatzidis, *Science*, 2016, **351**, 141.
- 5 (a) A. Assoud, S. Derakhshan, N. Soheilnia and H. Kleinke, *Chem. Mater.*, 2004, **16**, 4193; (b) A. Assoud, N. Soheilnia and H. Kleinke, *J. Solid State Chem.*, 2005, **178**, 1087; (c) A. Assoud and H. Kleinke, *Chem. Mater.*, 2005, **17**, 4509.
- 6 O. V. Dolomanov, L. J. Bourhis, R. J. Gildea, J. A. K. Howard and H. Puschmann, *J. Appl. Crystallogr.*, 2009, **42**, 339.
- 7 A. L. Spek, *J. Appl. Crystallogr.*, 2003, **36**, 7.
- 8 G. Kresse and D. Joubert, *Phys. Rev. B: Condens. Matter*, 1999, **59**, 1758.
- 9 P. E. Blochl, *Phys. Rev. B: Condens. Matter*, 1994, **50**, 17953.
- 10 J. P. Perdew, K. Burke and M. Ernzerhof, *Phys. Rev. Lett.*, 1996, **77**, 3865.
- 11 J. Heyd, G. E. Scuseria and M. Ernzerhof, *J. Chem. Phys.*, 2003, **118**, 8207.
- 12 A. A. Mostofi, J. R. Yates, Y. S. Lee, I. Souza, D. Vanderbilt and N. Marzari, *Comput. Phys. Commun.*, 2008, **178**, 685.
- 13 J. M. Jenks, J. T. Hoggins, L. E. Rendon, S. Cohen and H. Steinfink, *Inorg. Chem.*, 1978, **17**, 1773.
- 14 E. I. Rogacheva, G. V. Gorne, S. A. Laptev, A. V. Arinkin and T. B. Vesene, *Inorg. Mater.*, 1986, **22**, 34.
- 15 (a) P. Bottcher and U. Kretschmann, *Z. Anorg. Allg. Chem.*, 1982, **491**, 39; (b) P. Bottcher and U. Kretschmann, *J. Less-Common Met.*, 1983, **95**, 81; (c) J. Bernstein and R. Hoffmann, *Inorg. Chem.*, 1985, **24**, 4100.
- 16 X. F. Tang, W. J. Xie, H. Li, W. Y. Zhao, Q. J. Zhang and M. Niino, *Appl. Phys. Lett.*, 2007, **90**, 012102.